catalysts

MDPI

Article

Flower-Shaped C-Dots/Co_3O_4{111} Constructed with Dual-Reaction Centers for Enhancement of Fenton-Like Reaction Activity and Peroxymonosulfate Conversion to Sulfate Radical

Zhibin Wen [1,†], Qianqian Zhu [1,†], Jiali Zhou [1], Shudi Zhao [1], Jinnan Wang [1,*], Aimin Li [1], Lifang Chen [2] and Weilin Bian [2]

[1] State Key Laboratory of Pollution Control and Resource Reuse & School of the Environment Nanjing University, Nanjing 210023, China; wzb0215@126.com (Z.W.); qianqianzhunju@163.com (Q.Z.); m13160071912@163.com (J.Z.); cncd@163.com (S.Z.); liaimin@nju.edu.cn (A.L.)

[2] Institute of Water Environmental Engineering & Technology, Yancheng 224000, China; li-fang-chen@163.com (L.C.); bianweilin1987@163.com (W.B.)

* Correspondence: wjnnju@163.com; Tel.: +86-138-5153-4615

† Two authors made contributions equally.

Abstract: Novel flower-shaped C-dots/Co_3O_4{111} with dual-reaction centers were constructed to improve the Fenton-like reaction activity and peroxymonosulfate (PMS) conversion to sulfate radicals. Due to the exposure of a high surface area and Co_3O_4{111} facets, flower-shaped C-dots/Co_3O_4{111} could provide more Co(II) for PMS activation than traditional spherical Co_3O_4{110}. Meanwhile, PMS was preferred for adsorption on Co_3O_4{111} facets because of a high adsorption energy and thereby facilitated the electron transfer from Co(II) to PMS. More importantly, the Co–O–C linkage between C-dots and Co_3O_4{111} induced the formation of the dual-reaction center, which promoted the production of reactive organic radicals (R•). PMS could be directly reduced to SO_4^{-}• by R• over C-dots. On the other hand, electron transferred from R• to Co via Co–O–C linkage could accelerate the redox of Co(II)/(III), avoiding the invalid decomposition of PMS. Thus, C-dots doped on Co_3O_4{111} improved the PMS conversion rate to SO_4^{-}• over the single active site, resulting in high turnover numbers (TONs). In addition, TPR analysis indicated that the optimal content of C-dots doped on Co_3O_4{111} is 2.5%. More than 99% of antibiotics and dyes were degraded over C-dots/Co_3O_4{111} within 10 min. Even after six cycles, C-dots/Co_3O_4{111} still remained a high catalytic activity.

Keywords: C-dots/Co_3O_4{111}; dual-reaction centers; enhancement; peroxymonosulfate; conversion to sulfate radical

check for updates

Citation: Wen, Z.; Zhu, Q.; Zhou, J.; Zhao, S.; Wang, J.; Li, A.; Chen, L.; Bian, W. Flower-Shaped C-Dots/Co_3O_4{111} Constructed with Dual-Reaction Centers for Enhancement of Fenton-Like Reaction Activity and Peroxymonosulfate Conversion to Sulfate Radical. *Catalysts* **2021**, *11*, 135. https://doi.org/10.3390/catal11010135

Received: 24 December 2020
Accepted: 13 January 2021
Published: 18 January 2021

1. Introduction

Being attributed to higher oxidative potential (E^0 = 2.5–3.1 V) and longer half-life ($t_{1/2}$ = 30–40 μs), sulfate radical (SO_4^{-}•) could degrade organics more efficiently than OH• (E^0 = 2.80 V, $t_{1/2}$ = <1 μs) in neutral solutions. Generally, a Fenton-like reaction was significantly influenced by pH. In neutral/alkaline condition, transition metal ion might form precipitate, resulting in preventing the reaction. On the other hand, SO_4^{-}• could react with OH^- to produce OH• with lower oxidative ability. To enhance the peroxymonosulfate (PMS) conversion to SO_4^{-}•, various transition metals (Fe, Cu, Mn, and Co) were investigated as activator [1–3]. Among them, cobalt oxides [CoO, CoO_2, CoO(OH), Co_2O_3, and Co_3O_4] were considered as the most promising catalysts due to high standard reduction potential (E^0 = +1.92 V vs. NHE) and redox of Co(III)/Co(II) [1]. During the process of a Fenton-like reaction, PMS can not only react with Co(II) as the electron acceptor but also reacts with Co(III) as the electron donor, accompanied by the

circulation of Co(III)/Co(II) and the generation of SO_4^{-}• or SO_5^{-}• [4]. However, similar to classic Fenton reaction, the rate-limiting step [Co(III) + HSO_5^{-} → Co(II) + SO_5^{-}• + H^+] and low conversion PMS to SO_5^{-}• seriously restrict the application of cobalt oxides as catalysts [5]. In addition, the active components of catalysts might be converted into low activity substances during the reaction process due to poor stability. For example, cobalt oxides might be corroded and dissolved during the redox process, resulting in deterioration of catalytic performance.

In general, catalysts activity and stability could be influenced by surface morphology and crystal phase. Firstly, the mass transfer between organics and catalyst active sites was affected by the catalysts morphology. Li et al. constructed $Fe_xCo_{3-x}O_4$ with porous nanocages structure, which indicated that such morphology significantly improved the catalytic activity and stability [6]. Secondly, atoms arrangement of catalyst, which led to exposure of transition metal with different chemical value, was depended on the crystal structure [7,8]. As for Co_3O_4, both Co(III) and Co(II) occupied lattice point of octahedron {110} facet, while Co(II) entirely occupied the lattice point of tetrahedron {111} facet [8,9]. More importantly, different crystal facets possessed different adsorption energies and electrons transfer properties, which might directly influence the catalytic reaction. Hensen et al synthesized CeO_2 with different crystal planes to investigate its effect on CO oxidation, which found that the free energy barrier of Pd/CeO_2(100) for the CO catalytic cycle was higher than that of Pd/CeO_2(111) [10]. Thus, it is expected that Co_3O_4 constructed by tetrahedron{111} can not only provide more Co(II) for PMS activation, but also possess higher adsorption energies and electrons transfer properties for PMS activation.

On the other hand, although increase of Co(II) exposed can obviously improve the catalytic activity, Co(III) would be still accumulated in the system because of the rate limitation step [Co(III) + HSO_5^{-} → Co(II) + SO_5^{-}• + H^+] with the reaction time. Since the oxidative potential of SO_5^{-}• is relatively low, the degradation rate of organics by SO_5^{-}• is much lower than by SO_4^{-}•. Thus, the selective PMS conversion to SO_4^{-}• over cobalt oxides still remained to be improved. In general, cation–π interaction could be formed between the cations and aromatic systems, which could be applied in the classic Fenton system for improvement of transition metal redox [11]. Zubir et al. demonstrated that unpaired π electrons of GO could transfer electrons between GO and iron centers via cation–π interactions, which significantly improved the recyclability of Fe_3O_4 [12]. In addition, the active transition complex [C-H_2O_2], which was formed between covalent carbon networks and H_2O_2, can directly transfer electron from the π-system to H_2O_2 with the generation of OH• [13]. Analogous to g-C_3N_4, carbon quantum dots (C-dots) are considered as a potential carbon-based co-catalyst due to their graphene structure [14,15]. Wang et al. synthesized the SiO_2@C-dots/phosphotungstate catalyst with an inert SiO_2 core and a catalytic active shell made up of the prepared amphiphilic phosphotungstate and C-dots, which proved that C-dots were an efficient co-catalyst in the system [16]. Our previous work also demonstrated that an electron-rich Cu center and electron-deficient π-electron conjugated system could be constructed by doping of g-C_3N_4 in Cu-Al_2O_3, which provided two electron-transfer routes for OH• generation in the presence of H_2O_2 [11]. Meanwhile, addition of C-dots in the hydrothermal system could modulate the formation of crystal structure because of the large number of oxygen functional groups on the surface of C-dots, which act as "surfactants". Thus, it is expected to simultaneously enhance the catalytic activity and selective PMS conversion to SO_4^{-}• by doping of C-dots into Co_3O_4{111}. Notably, C-dots can improve the production of reactive organic radicals (R•) from the reaction of SO_4^{-}• and organics. Such reactive organic radicals play an important role in the enhancement of catalytic activity and selective PMS conversion to SO_4^{-}•. Some of electrons can be transferred from R• to Co(III) via Co–O–C linkage for Co(III) reduction to Co(II) without PMS decomposition, and other electrons can be transferred from R• to PMS over C-dots with the generation of SO_4^{-}•.

Based on the above research background and conception, flower-shaped C-dots/Co_3O_4 {111} with high active crystal facets are constructed for improvement of catalytic activity

and selective PMS conversion to SO_4^{-}•. Being attributed to {111} facets, flower-shaped C-dots/Co_3O_4{111} could not only provide large amounts of Co(II) but also possess higher adsorption energies and electrons transfer properties for PMS reduction to SO_4^{-}•. More importantly, doping of C-dots on Co_3O_4{111} could facilitate the production of reactive organic radicals (R•) which can act as the important electron donor. On one hand, Co(III) in C-dots/Co_3O_4{111} can be reduced to Co(II) by oxidation of R•. On the other hand, SO_4^{-}• can be generated from the reaction of PMS and R• over C-dots. Such synergistic effect significantly improved PMS activation and selective conversion to SO_4^{-}•.

2. Results and Discussion

2.1. Characterization of Catalysts

Cetrimonium Bromide (CTMAB) showed significant influence on the surface morphology of Co_3O_4 during the hydrothermal reaction process. Co_3O_4 synthesized by hydrothermal reaction without CTMAB are spherical particles with the diameter of 2 μm (Figure 1a). However, due to a decrease of the surface energy, ethanol and cobalt salts could form nano-sheets in the present of CTMAB. Thus, the product of Co_3O_4 and C-dots/Co_3O_4{111}, which are synthesized in the present of CTMAB, shows a flower-shaped structure (diameter = 5 μm) with a nano-sheets thickness of 67 nm (Figure 1b,c). Notably, the flower-shaped structure increased the surface area and pore volume of catalyst, which could be confirmed by the results of the BET surface area (Table 1). The BET surface area of flower-shaped C-dots/Co_3O_4{111} was 109.11 m^2/g, which was much higher than that of spherical Co_3O_4{110} (35.45 m^2/g). A large specific surface area is beneficial to improving the catalytic activity of the catalyst.

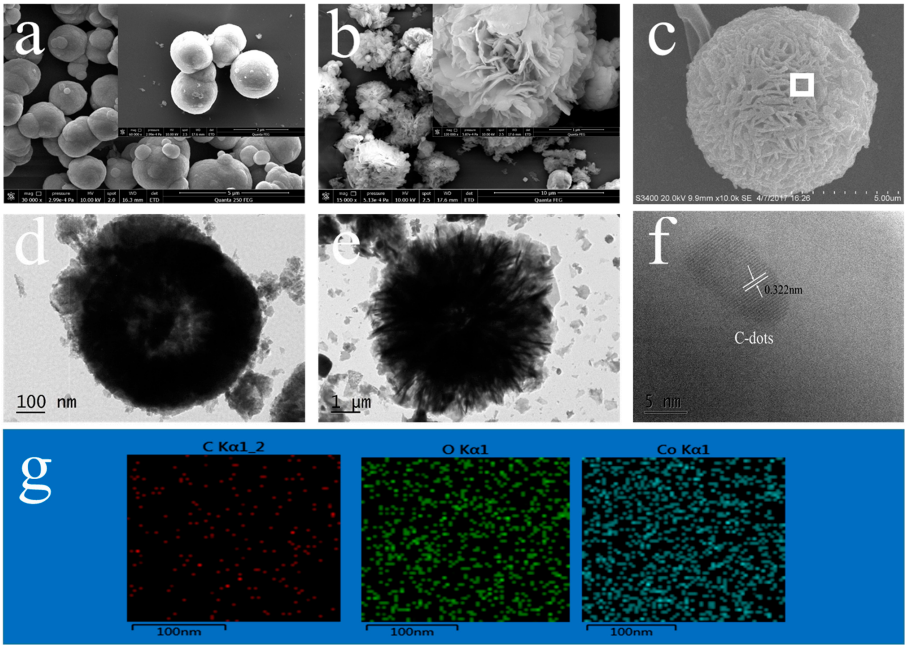

Figure 1. SEM image of (**a**) spherical Co_3O_4{110}, (**b**) flower-shaped Co_3O_4{111}, and (**c**) flower-shaped C-dots/Co_3O_4{111}; TEM image of (**d**) spherical Co_3O_4{110}, (**e**) flower-shaped Co_3O_4{111}, and (**f**) flower-shaped C-dots/Co_3O_4{111}; (**g**) EDS of flower-shaped C-dots/Co_3O_4{111}.

Furthermore, as shown in TEM (Figure 1d), the 'd' spacing of lattice fringe corresponding to (111) and (220) planes of spherical Co_3O_4 are respectively 0.464 nm and 0.284 nm, and the inter planar angles between these two planes are 90°, suggesting the {110} crystal structure of the spherical Co_3O_4 [17]. Different from spherical Co_3O_4{110}, the 'd' spacing of lattice fringe corresponding to (220) and (442) planes of flower-shaped Co_3O_4{111} are respectively 0.286 nm and 0.167 nm (Figure 1e), and the inter planar angle between these two planes is 30°, suggesting the {111} crystal structure of flower-shaped Co_3O_4{111} [18].

Such difference between spherical Co_3O_4{110} and flower-shaped Co_3O_4{111} was due to that surfactants were preferentially adsorbed on crystal faces, which limited the directional growth of nanocrystals and stabilizing the crystal faces. Various ordered aggregates formed by self-assembly of surfactants in solution can be used as microreactors or templates, which could control the morphology of nano-materials [19]. Thus, addition of CTMAB probably played the dominant role in the formation of {111} crystal structure of Co_3O_4 during the process of hydrothermal reaction. In addition, TEM images (Figure 1f) confirm that the C-dots are successfully doped in the flower-shaped Co_3O_4{111} in which the lattice fringes spacing of 0.322 nm is in accordance with the (002) lattice planes of graphitic carbon [20]. EDS images further demonstrate that the C element is homogenously distributed on the catalyst surfaces (Figure 1g), which show that the C-dots are uniformly doped on Co_3O_4.

Table 1. The BET specific surface area, total pore volume, and average pore diameter of catalysts prepared.

Catalyst	BET Specific Surface Area (m^2/g)	Total Pore Volume (cm^3/g)	Average Pore Diameter (Å)
Spherical Co_3O_4{110}	35.45	0.045	66.91
Flower-shaped Co_3O_4{111}	83.01	0.092	76.25
Flower-shaped C-dots/Co_3O_4{111}	109.11	0.107	68.6

XRD spectra clearly describe the crystal structure of catalysts synthesized under different hydrothermal reaction conditions (Figure 2a). The diffraction peaks at 31.4°, 37.1°, 44.9°, 55.9°, 59.7°, and 65.2° were respectively ascribed to the [220], [311], [400], [442], [511], and [440] diffraction planes of Co_3O_4, which could be indexed to a pure phase of spinel Co_3O_4 (JCPDS card NO.43-1003). Since there was no impurity peaks in XRD spectra, which could confirm the excellent crystalline of flower-shaped Co_3O_4{111}, spherical Co_3O_4{110}, and flower-shaped C-dots/Co_3O_4{111} [21]. In general, the Co_3O_4 crystal is a typical spinel structure ($Co^{2+}(Co^{3+})_2O_{2-4}$), which consists of octahedron (CoO_6) and tetrahedron (CoO_4). Notably, Co(III) species are located in octahedral sites while Co(II) species are in tetrahedral sites (Figure 2b). Since Co(II) is the catalytic site for PMS select conversion to SO_4^{-}• [22], tetrahedron structure (CoO_4) with more Co(II) exposed can provide more catalytic sites for PMS activation. Therefore, in perspective of atomic arrangement, accessible Co(II) with PMS is beneficial for improvement of catalytic activity. To a certain degree, it can be considered that the tetrahedron structure (CoO_4) shows higher catalytic activity compared with octahedron structure (CoO_6).

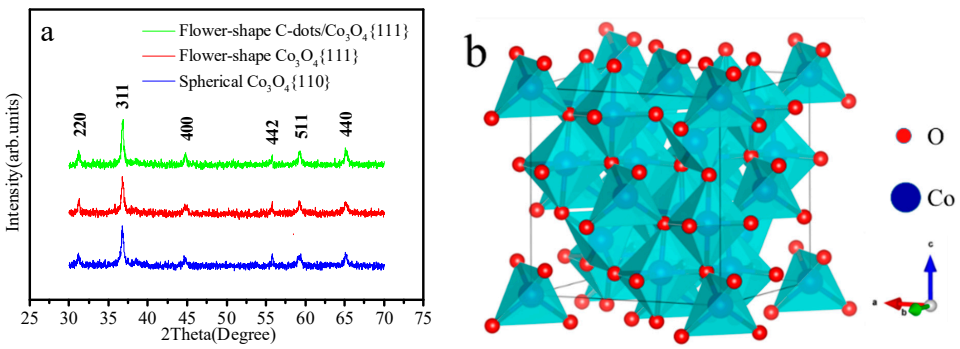

Figure 2. (**a**) XRD patterns of different catalysts, (**b**) schematic representation of spinel structure of Co_3O_4.

Furthermore, XPS was used to characterize the surface composition and chemical state of flower-shaped Co_3O_4{111}, spherical Co_3O_4{110}, and flower-shaped C-dots/Co_3O_4{111} (Figure 3 and Figure S1). The binding energy peaks near 780 and 795 eV are ascribed to orbits of Co $2p_{1/2}$ and Co$2p_{3/2}$, respectively (Figure 3a,c,e). The orbital peak of Co

$2p_{3/2}$ can be further separated into two peaks of Co^{3+} (779.8 eV) and Co^{2+} (781.1 eV). Then, the value of Co(II)/Co(III) on the catalysts surface can be calculated according to the peaks area of different valence state of Co (Table 2). The proportion of Co(II) on the surface of flower-shaped Co_3O_4{111} [Co(II)/Co(III) = 1.36] and C-dots/Co_3O_4{111} [Co(II)/Co(III) = 1.36] are much higher than that on spherical Co_3O_4{110} [Co(II)/Co(III) = 0.77]. Thus, compared with spherical Co_3O_4{110}, more active sites of Co(II), which plays the role of activating PMS, were exposed on the surface of flower-shaped Co_3O_4{111} and C-dots/Co_3O_4{111}. In addition, the orbital peak of O 1s can be separated into three peaks. The binding energy of 529 ± 0.2 eV was the characteristic peak of lattice oxygen (O_L) in the Co_3O_4 phase. The peak of O_V (531 ± 0.1 eV) was ascribed to the O^{2-} in oxygen-deficient regions within the matrix of Co_3O_4, and the peak of O_C (532 ± 0.2 eV) was ascribed to OH^-, chemisorbed or dissociated oxygen species (O^{2-}, O_2^-, or O^-). Notably, the value of O_C/O_L of flower-shaped C-dots/Co_3O_4{111} was much higher than those of flower-shaped Co_3O_4{111} and spherical Co_3O_4{110}, which indicated that doping C-dots into Co_3O_4 increased the oxygen functional groups on the surface of the catalyst. Since oxygen functional groups on nano-carbons can act as the catalytic sites for PMS activation to generate radicals. Since occupation of the binding sites by surface hydroxyl sites of catalyst could facilitate the oxidation reactions [22], doping of C-dots into Co_3O_4{111} could improve the catalytic performance.

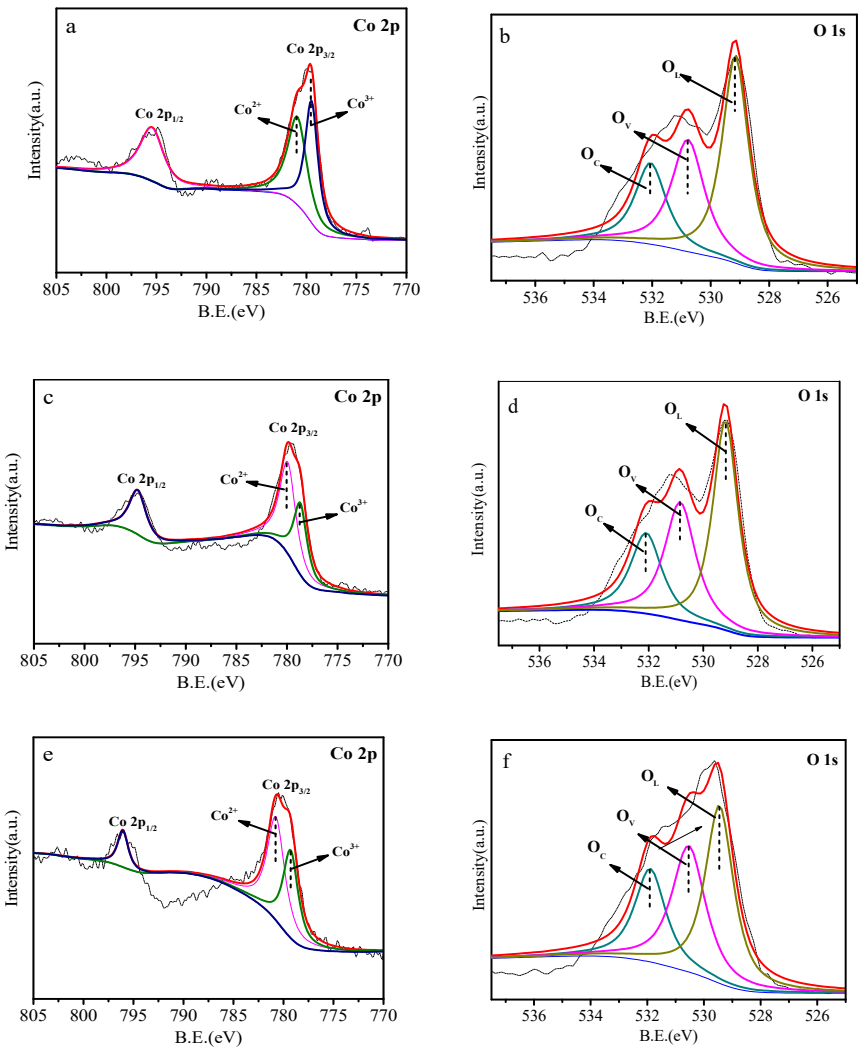

Figure 3. XPS spectra of catalysts, Co2p of (**a**) spherical Co_3O_4, (**c**) flower-shaped Co_3O_4, (**e**) flower-shaped C-dots/Co_3O_4{111}; O 1s peaks of (**b**) spherical Co_3O_4, (**d**) flower-shaped Co_3O_4, (**f**) flower-shaped C-dots/Co_3O_4{111}.

Table 2. Element molar ratios [Co(II)/Co(III)] on the surface of different catalysts.

Samples	Binding Energy (eV)				Ratios	
	Co(II)	Co(III)	O_C	O_L	Co(II)/Co(III)	O_C/O_L
Spherical Co_3O_4{110}	779.8	781.1	532.1	529.1	0.77	0.659
Flower-shaped Co_3O_4{111}	779.6	781	532	529	1.36	0.635
Flower-shaped C-dots/Co_3O_4{111}	779.8	781.2	532.1	529.1	1.36	0.844

FT-IR spectra can demonstrate the functional groups of spherical Co_3O_4{110}, flower-shaped Co_3O_4{111}, and flower-shaped C-dots/Co_3O_4{111} (Figure 4a). The characteristic peaks at 574.69 cm^{-1} and 661.48 cm^{-1} are assigned to the stretching vibrations of Co–O groups of Co_3O_4, and the peak at 3557 cm^{-1} belongs to the free O–H stretching vibration [23]. In addition, peaks near 1633.4 cm^{-1} of samples are related to the bending –OH vibrations of physical adsorbed water [24,25]. Furthermore, the bands in the range of 1490.73 cm^{-1} are ascribed to the C=C aromatic stretching vibrations. The bands at 1307.52 and 1000.89 cm^{-1} correspond to the C−O stretching absorption and COO– functional groups, respectively. According to the results of XPS and FT-IR, doping of C-dots greatly enriched the oxygen functional groups (–OH, C=O) on the Co_3O_4 surface, which could significantly improve the catalytic performance of the catalyst.

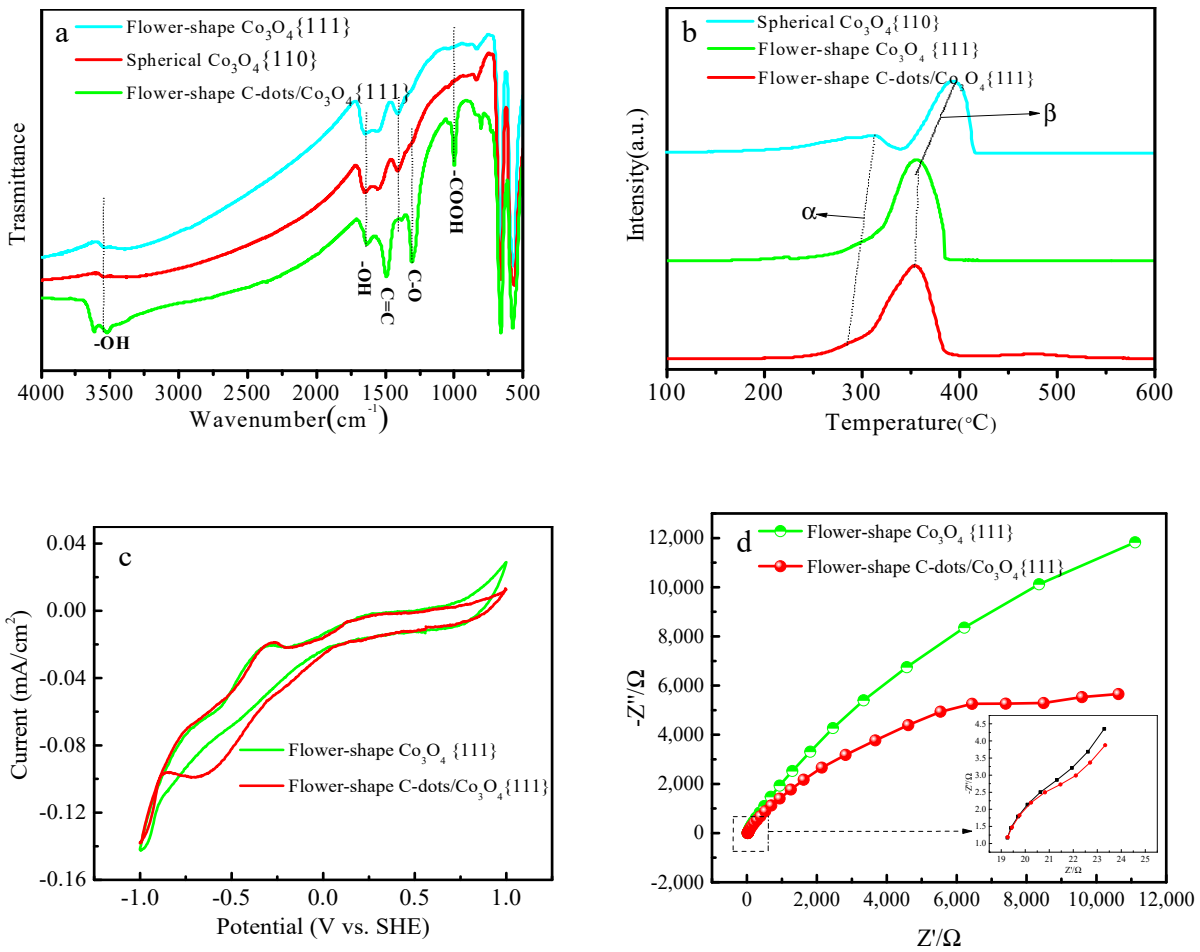

Figure 4. (**a**) The FT−IR spectrum of spherical Co_3O_4, flower-shaped Co_3O_4{111}, and flower-shaped C-dots/Co_3O_4{111}, (**b**) H_2-TPR profiles of Co_3O_4 catalysts with different conditions, (**c**) cyclic voltammetry (CV) curves of the as−prepared flower-shaped Co_3O_4{111}, and flower-shaped C-dots/Co_3O_4{111}, (**d**) EIS Nyquist plots collected at −0.3 V vs. Ag/AgCl.

The redox properties of catalysts were characterized by the H_2-TPR (Figure 4b). The β peak represents the reduction of Co(II) to Co^0 in Co_3O_4 (Equation (2)), while the α peak represents the reduction of Co(III) to Co(II) (Equation (3)). The α peak and β peak of spherical Co_3O_4{110} are 319 °C and 398 °C, respectively. Due to the oxygen vacancy on the surface of flower-shaped Co_3O_4{111} and C-dots/Co_3O_4{111} (Figure S3), the reduction temperature ($Co^{2+} \rightarrow Co^0$, $Co^{3+} \rightarrow Co^{2+}$) decreased obviously. The surface oxygen vacancy can promote the reduction of the catalyst, which leads to the reduction of the flower-shaped Co_3O_4{111} and C-dots/Co_3O_4{111} at the lower temperature. In addition, the α peak intensity of flower-shaped Co_3O_4{111} and C-dots/Co_3O_4{111} are much lower than that of spherical Co_3O_4{110}. The area ratio of α peak to β peak of spherical Co_3O_4{110} is 0.31 by calculation, while that of flower-shaped Co_3O_4{111} and C-dots/Co_3O_4{111} is only 0.27, which confirmed that there are more CoO contents in flower-shaped Co_3O_4{111} and C-dots/Co_3O_4{111} crystal compared with spherical Co_3O_4{110}. In addition, TPR results of flower-shaped C-dots/Co_3O_4{111} with different C-dots amounts are provided to explore the optimal doping of C-dots for PMS activation (Figure S2). The temperature of Co^{3+} reduction to Co^{2+} decreases gradually as the C-dots content increase from 0.5% to 2.5%, which indicates that doping of C-dots can improve the reducibility of Co_3O_4{111}. However, the temperature of Co^{3+} reduction to Co^{2+} increases as the C-dots content increased from 2.5% to 3.5%, suggesting that excessive doping of C-dots weaken the reduction ability of Co_3O_4. Similar results are also observed in TPR results of Co^{2+} reduction to Co^0. Such adverse effect can be explained by that excess C-dots could cover the surface of the catalyst, resulting in the inhibition of the Co_3O_4 reduction by H_2. Thus, C-dots (2.5%)/Co_3O_4{111} were selected for further studies.

Cyclic voltammetry (CV) was used to test the charge transfer at the interfacial region of Co_3O_4/PMS in a three-electrode system (Figure 4c). Ag/AgCl was used as reference electrode, platinum was used as pair electrodes, and glassy carbon was used as working electrode. The mixture of 0.1 M Na_2SO_4 and 0.3 mM PMS was used as electrolyte. The CV curves of flower-shaped Co_3O_4{111} and flower-shaped C-dots/Co_3O_4{111} showed distinct reduction peaks beginning at a low potential of −0.25 V (Figure 4c). These reduction peaks indicated that the surface C-dots served as the active sites for the PMS activation. Compared with flower-shaped Co_3O_4{111}, flower-shaped C-dots/Co_3O_4{111} have a higher current density in the cathode, suggesting that C-dots can transfer electrons to PMS. In addition, compared with flower-shaped Co_3O_4{111}, flower-shaped C-dots/Co_3O_4{111} show the smaller semicircle within a higher frequency region in the EIS Nyquist plots (Figure 4d). Due to the similar graphene structure of C-dots, the Dirac Point effect improved the electron transfer of C-dots. Thus, C-dots doped on flower-shaped Co_3O_4{111} could accelerate the redox cycle of Co(II)/Co(III).

$$3CoO + 3H_2 \rightarrow 3Co + 3H_2O, \quad (1)$$

$$Co_3O_4 + H_2 \rightarrow 3CoO + H_2O. \quad (2)$$

2.2. Catalytic Activity and Stability

The degradation rate of OTC and ENR by PMS over flower-shaped C-dots/Co_3O_4{111} are much higher than that over other catalysts (Figure 5a,c). More than 99.3% OTC was degraded in 5 min (PMS = 0.075 mM), while more than 99.7% ENR was degraded in 10 min over the flower-shaped C-dots(2.0 wt%)/Co_3O_4{111} (PMS = 0.3 mM). The degradation kinetics by PMS over various catalysts can be well described by pseudo-first-order kinetic model ($-lnC/C_0 = kt$), where 'C_0' is the initial concentration of OTC, 'C' is the concentration of reactant at time 't', and 'k' is the rate constant. The rate constants followed the order of flower-shaped C-dots/Co_3O_4{111} > flower-shaped Co_3O_4{111} > spherical Co_3O_4{110} (Table S1). Notably, the rate constant of flower-shaped C-dots/Co_3O_4{111} is four times higher than spherical Co_3O_4{110} and flower-shaped Co_3O_4{111} (Figure 5b,d). Accordingly, the addition of C-dots could obviously improve the catalytic activity of Co_3O_4. The optimal content of C-dots doped in flower-shaped Co_3O_4{111} was 2%.

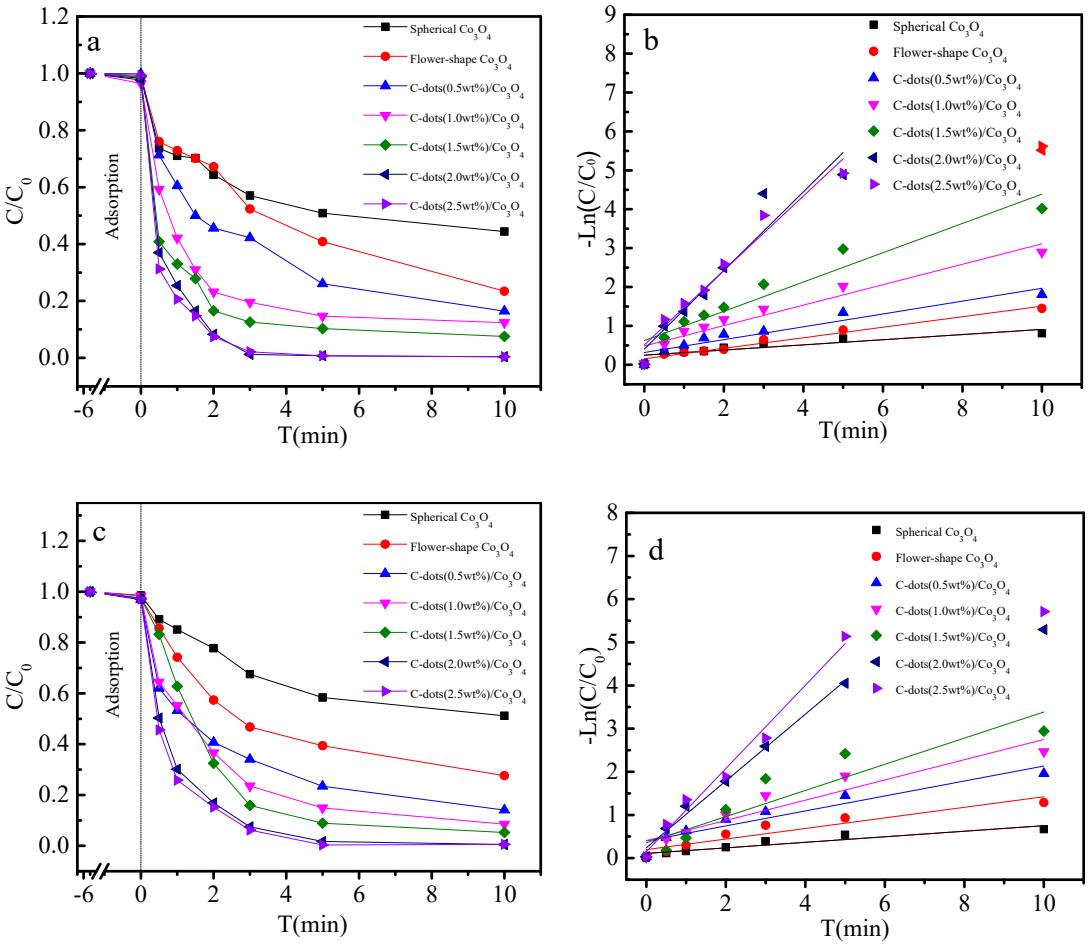

Figure 5. Degradation of (**a**) Oxytetracycline (OTC) and (**c**) Enrofloxacin (ENR) in the presence of flower-shaped C-dots/Co_3O_4{111} and PMS (pH = 7.00 with 0.075 mM/0.3 mM peroxymonosulfate (PMS), 0.05 g/L catalyst dosage, and 10 ppm OTC/ENR (200 mL)); pseudo-first-order kinetic model fits the degradation kinetic curves of (**b**) OTC and (**d**) ENR.

The influences of catalyst dosage and oxidant concentration on the catalytic degradation of ENR were tested. The degradation rate of ENR increases from 56.4% to 99.4% within 10 min while the dosage of flower-shaped C-dots/Co_3O_4{111} increases from 0.01 to 0.05 $g \cdot L^{-1}$ (Figure S3a). This was because an increase of the catalysts dosage could supply more active sites for catalytic generation of radicals, which promoted the antibiotics degradation. Similar to the catalyst dosage, the increase of PMS concentration can also improve the degradation of ENR (Figure S3b). As the PMS concentration increased from 0.05 to 0.3 mM, the removal rate of ENR increased from 74.2% to 99.8% within 10 min. Since the generation rate of the radicals was related to the catalyst dosage, further increase of PMS concentration from 0.3 to 0.7 mM could not obviously improve the removal rate of ENR anymore. Therefore, the optimal concentration of PMS for ENR degradation was 0.3 mM.

Since high temperature is beneficial to PMS activation and generation of radicals, the removal rate of ENR obviously increases as the temperature increases from 25 °C to 55 °C (Figure S3c). The degradation kinetic constants also followed the order of $K_{55\,°C}$ (2.837 min^{-1}) > $K_{45\,°C}$ (1.355 min^{-1}) > $K_{35\,°C}$ (0.913 min^{-1}) > $K_{25\,°C}$ (0.469 min^{-1}). More than 99% of ENR could be degraded at 25 °C within 10 min. In consideration of energy consumption, the room temperature (25 °C) was selected for subsequent catalytic degradation experiments. Furthermore, due to changing the surface charge of catalyst, solution pH also influenced the degradation process obviously. The degradation rate of ENR increases as the initial solution pH increases from 3.0 to 6.0 (Figure S3d). Only 50% of ENR was removed at pH 3.0 within 20 min while ENR was almost completely degraded at pH 6.0. This is

because that Co leached from flower-shaped C-dots/Co_3O_4{111} in acid conditions was unfavorable to PMS activation. Notably, the concentrations of Co leached from catalysts in solution could meet the limit of Environmental Quality Standards for Surface Water in China (1.0 mg/L) (Figure S4). However, the degradation rate of ENR decreases as pH increases from 6.0 to 9.0, which indicated that alkaline conditions made adverse effect to catalytic degradation. This was because the large amount of OH^- reacted with SO_4^-• to generate OH•, resulting in lower oxidation ability in neutral/basic conditions.

In order to evaluate the reusability of flower-shaped C-dots/Co_3O_4{111}, OTC (10 mg/L), and ENR(10 mg/L) solutions are used to further test the catalytic degradation stability of C-dots/Co_3O_4{111} in the present work (Figure 6a,b). After six cycling runs, the degradation rate of OTC was still more than 90% within 2 min, and even 100% within 5 min (Figure 6a). Furthermore, the degradation kinetics did not decrease after the sixth cycle runs, showing a perfect catalytic stability of flower-shaped C-dots/Co_3O_4{111}. Similar to catalytic degradation of OTC, flower-shaped C-dots/Co_3O_4{111} also show high catalytic degradation rate of ENR, Rh B, and MB even after six cycles (Figure 6b–d), which also confirm the excellent stability of flower-shaped C-dots/Co_3O_4{111} for PMS activation.

In addition, the surface state of catalyst after six cycling runs is characterized by XPS spectra (Figure 6e). In this work, we propose that Co–O–C bonds conjugated in flower-shaped C-dots/Co_3O_4{111} facilitate electron transfer and correlate well with the transformation from R to R•. Such synergistic interaction between C-dots and Co_3O_4{111} could accelerate the Co(III)→Co(II) redox cycles. The bridge role played by C-dots could transfer electrons to Co(III) for its quick reduction as organic pollutants are oxidized [12]. XPS spectra of catalysts before and after reaction confirmed this inference. The value of Co(II)/Co(III) of flower-shaped C-dots/Co_3O_4{111} did not decreased after catalytic reaction (Figure 6f), which indicated that Co(II) was not oxidized to Co(III). This synergistic effect can not only effectively maintain the number of active sites of catalysts, but also reduce the ineffective decomposition of PMS. As for flower-shaped Co_3O_4{111}, the value of Co(II)/Co(III) decreased from 1.36 to 1.16 obviously after cycled uses (Figure 6f), indicating that some Co(II) of flower-shaped Co_3O_4{111} was oxidized to Co(III). Previous studies have already demonstrated that Co(II) play important role in PMS activation for generation of sulfate radicals. Thus, compared with flower-shaped Co_3O_4{111}, flower-shaped C-dots/Co_3O_4{111} showed higher catalytic activity and selective peroxymonosulfate (PMS) conversion to sulfate radicals.

2.3. Density Functional Theory (DFT) Calculation

In general, adsorption of PMS on catalysts was the premise of activation process. According to the density functional theory (DFT), the adsorption energy of PMS on {110} and {111} facets of Co_3O_4 are calculated by using the Materials Studio 7.0 CASTEP program (Figure S5). The convergence criteria were as follows: the maximal force on the atoms was 0.03 eV $Å^{-1}$, the stress on the atomic nuclei was less than 0.05 GPa, the maximal atomic displacement was 0.001 Å, and the maximal energy change per atom was 1.0 e^{-5} eV. The adsorption energy of PMS (E_{abs}) on Co_3O_4 can be calculated by the equation of $E_{ads} = E_{PMS+Cat} - E_{abs} - E_{Cat}$, where $E_{PMS+Cat}$, E_{abs}, and E_{Cat} refer to the energy of the optimized adsorption system, PMS and Co_3O_4, respectively. To obtain accurate results, we optimized the atomic coordinates by minimizing the total energy and atomic forces. The optimum adsorption energy of PMS on {110} and {111} facets are −1.12 eV and −5.97 eV, respectively, suggesting that PMS are preferred to be adsorbed on Co_3O_4{111} facet than on Co_3O_4{110} facet. Moreover, the total charge of PMS adsorbed on {111} facet (−0.32 e) was higher than that on {110} facet (−0.16 e), which also indicated that PMS can obtain more electrons from Co_3O_4{111} for activation. Thus, Co_3O_4{111} can exhibit higher catalytic activity and selective peroxymonosulfate (PMS) conversion to sulfate radical.

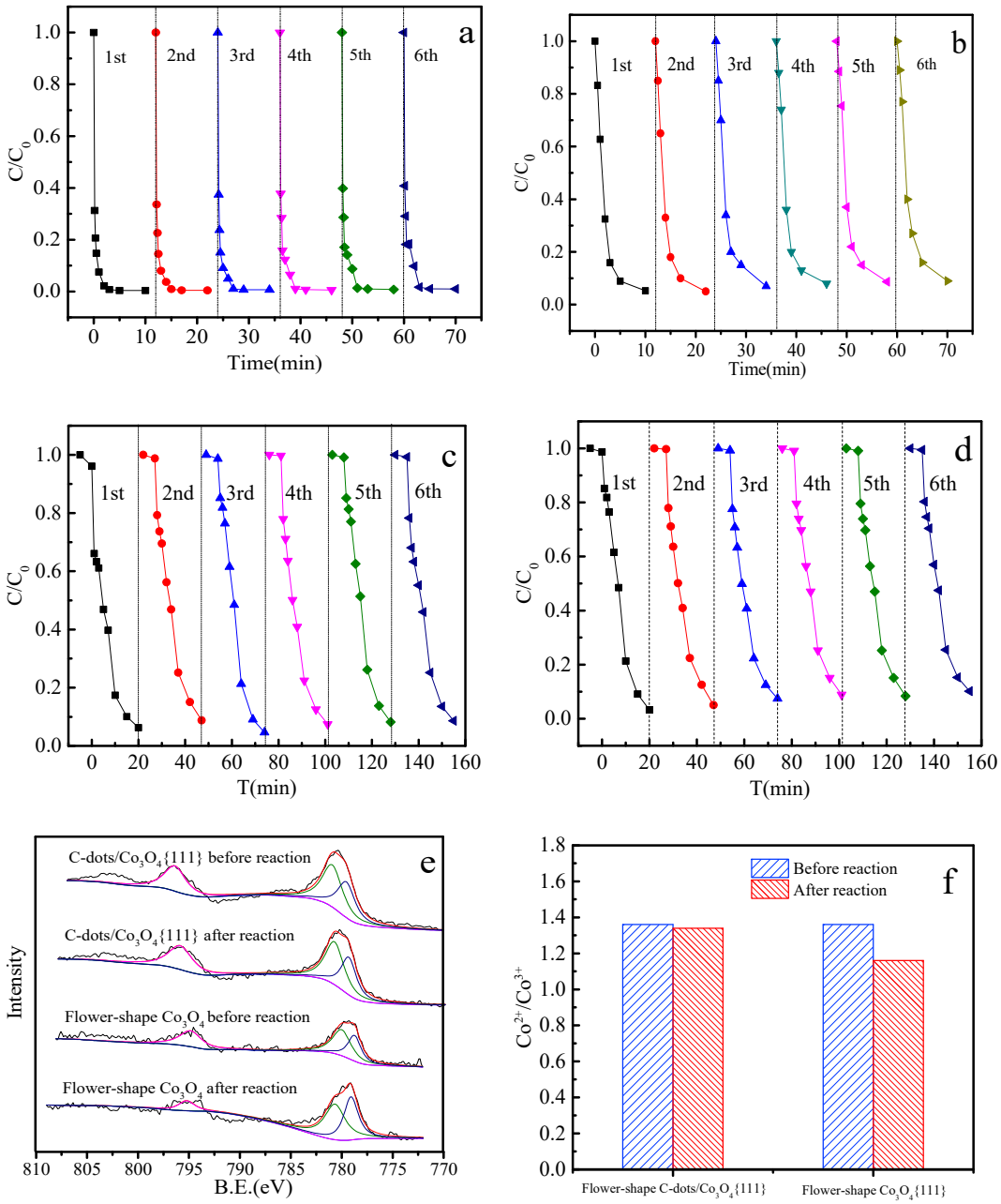

Figure 6. Cyclic performance of flower-shaped C-dots/Co_3O_4{111} for degradation of (**a**) OTC, (**b**) ENR, (**c**) Rh B, and (**d**) Methyl orange (MO) (pH = 7.00, PMS: 0.075/0.3 mM, C-dots/Co_3O_4{111}: 0.05 g/L, pollutant concentration:10 ppm (200 mL)); the (**e**) Co 2p XPS spectra of different catalysts before and after 6 cycling degradation of ENR. (**f**) Co^{2+}/Co^{3+} ratio based on XPS analysis.

2.4. The Possible Degradation Pathway of OTC and ENR

Generally, the unsaturated bonds of organic pollutants are easy to be broken in catalytic oxidation process. Based on the Frontier Orbital Theory, the highest occupied molecular orbital (HOMO) acts as the electron donor because of its weak binding force to electrons, while lowest unoccupied molecular orbital (LUMO) acts as electrons acceptor because of its strong binding force to electrons. In the present work, we calculated the bond energy of OTC and ENR by using Gaussian program, which indicates that the overlap of electronic clouds in LUMO and HOMO obviously influence the separation of e^- and h^+ (Figure S6). The large density of the electron cloud in OTC is mainly in the area of 1C, 9C, 14C, 24N. In the case of ENR, the electronic cloud mainly distributed in 3C, 6C, 19C,

20C. The active sites of pollutants were greatly contributed by the frontier orbitals, and unsaturated bonds strongly influenced the activity of antibiotic molecules. Thus, bonds in these positions of ENR and OTC are broken preferentially. In addition, the electron cloud density of OTC is much greater than that of ENR, which caused a higher degradation rate of OTC compared with ENR.

Furthermore, the intermediates of OTC and ENR degradation are identified by LC-MS/TOF, and iron spectra at different retention time (RT) are presented in ESI Scan (Figures S7 and S8). As for OTC degradation intermediates, the original iron at m/z = 461.1($[M + H]^+$) could be identified as $C_{22}H_{24}N_2O_9$. Furthermore, from the mass spectra, some other peaks appeared as the degradation of OTC, which suggested that there were other intermediate products produced. These main products irons at m/z = 460.2 ($[M + H]^+$), m/z = 434.2 ($[M + H]^+$), m/z = 447.2 ($[M + H]^+$), m/z = 432.2 ($[M + H]^+$), m/z = 347.2 ($[M + H]^+$), and m/z = 218.2 ($[M + H]^+$) might be identified as $C_{22}H_{24}N_2O_9$, $C_{22}H_{28}NO_8$, $C_{22}H_{27}N_2O_8$, $C_{22}H_{26}NO_8$, $C_{19}H_{25}NO_5$, $C_{12}H_{27}NO_2$, and $C_9H_6O_4$, respectively. In addition, m/z = 194.1 ($[M + H]^+$) might be identified as $C_{12}H_{18}O_2$ or $C_{11}H_{14}O_3$ [20,26–29]. Finally, all these substances were thoroughly decomposed into CO_2, H_2O, and other gaseous components. Similarly, iron spectra at different retention time (RT) of ENR degradation are presented in ESI Scan (Figure S8). The original iron at m/z = 360.2($[M + H]^+$) can be identified as $C_{19}H_{22}FN_3O_3$. These main product irons at m/z = 344.3($[M + H]^+$), m/z = 332.2 ($[M + H]^+$), m/z = 361.1 ($[M + H]^+$), m/z = 242.3 ($[M + H]^+$), m/z = 174.2 ($[M + H]^+$), m/z = 202.2 ($[M + H]^+$), and m/z = 102.1 ($[M + H]^+$) might be identified as $C_{19}H_{23}N_3O_3$, $C_{17}H_{18}FN_3O_3$, $C_{17}H_{15}FN_3O_5$, $C_{13}H_{10}N_2O_3$, $C_7H_{13}N_2O_3$, $C_{10}H_5N_2O_3$, and $C_5H_9O_2$; m/z = 302.2 ($[M + H]^+$) might be identified as $C_{16}H_{19}N_3O_3$ or $C_{16}H_{22}N_3O_2$; and m/z = 192.2 ($[M + H]^+$) might be identified as $C_{17}H_{24}FN_3O_2$ or $C_{10}H_{11}N_2O_3$ [30–33]. Finally, these substances were decomposed to CO_2, H_2O, and other gaseous components. TOC removal over different catalyst is shown in Figure S9, which indicates that more that 60% organics are mineralized over flower-shaped C-dots/Co_3O_4{111}. Based on the above results, the possible catalytic degradation pathways of OTC and ENR are proposed (Figure 7).

2.5. Proposed Catalytic Mechanism

Generally, sulfate radicals (SO_4^{-}•) and hydroxyl radicals (OH•) are considered as the most important radicals for degradation of organic pollutants in the PMS activation system [34–36]. To identify which radical played the dominant role for the ENR degradation, classic quenching tests were carried out in which ethanol (EtOH) and tert-Butanol (TBA) were used as radical scavenger. In different quenching conditions, the reaction rate constants of sulfate radical and hydroxyl radical are shown in Table 3 [37,38]. As shown in Figure 8a, about 100% of ENR is degraded in 15 min in the absence of scavenger, while the degradation of ENR obviously decreased as the TBA was added in. Notably, compared with TBA, EtOH showed stronger inhibition to catalytic degradation of ENR. Thus, both hydroxyl radical and sulfate radical played the important role in catalytic degradation process.

To further elucidate the catalytic mechanism, DMPO-trapped EPR signals were detected in different aqueous dispersions of the corresponding samples with the addition of PMS (Figure 8). In the absence of catalysts, signals were not observed in the system of DMPO/PMS/ENR dispersion and the blank experiment (Figure S10). As flower-shaped C-dots/Co_3O_4{111} were added, characteristic signals of DMPO-OH and DMPO-SO_4 were still not observed. However, unexpected characteristic signals which were ascribed to the oxidation products of DMPO (DMPOX) with the intensity ratios of 1:2:1:2:1:2:1 were captured (Figure S10). Since the dosage of oxidant (PMS) was more than pollutants (ENR), the excessive PMS would generate active substance/radicals (OH•, SO_4^{-}•, H_2O_2) which could oxidize DMPO to DMPOX [34,39]. As the PMS dosage decreased to 1.67 g/L, the characteristic peaks of DMPO-OH adduct (with hyperfine splitting constants of $\alpha_N = \alpha_H$ = 14.6 G) and DMPO-SO_4 adducts (with hyperfine splitting constants of α_N = 12.7 G, αα H = 10.3 G, αβ H = 2.1 G, αγ H = 1.1 G) are observed, revealing the simultaneous presence

of OH• and SO_4^-•. The characteristic peaks of DMPO–SO_4^-• and DMPO-OH• were observed in the dispersions of catalysts with their intensities following the order of flower-shape C-dots/Co_3O_4{111} > flower-shaped Co_3O_4{111} > spherical Co_3O_4{110}, which indicated that doping C-dots on Co_3O_4{111} could effectively improve the generation of sulfate radicals.

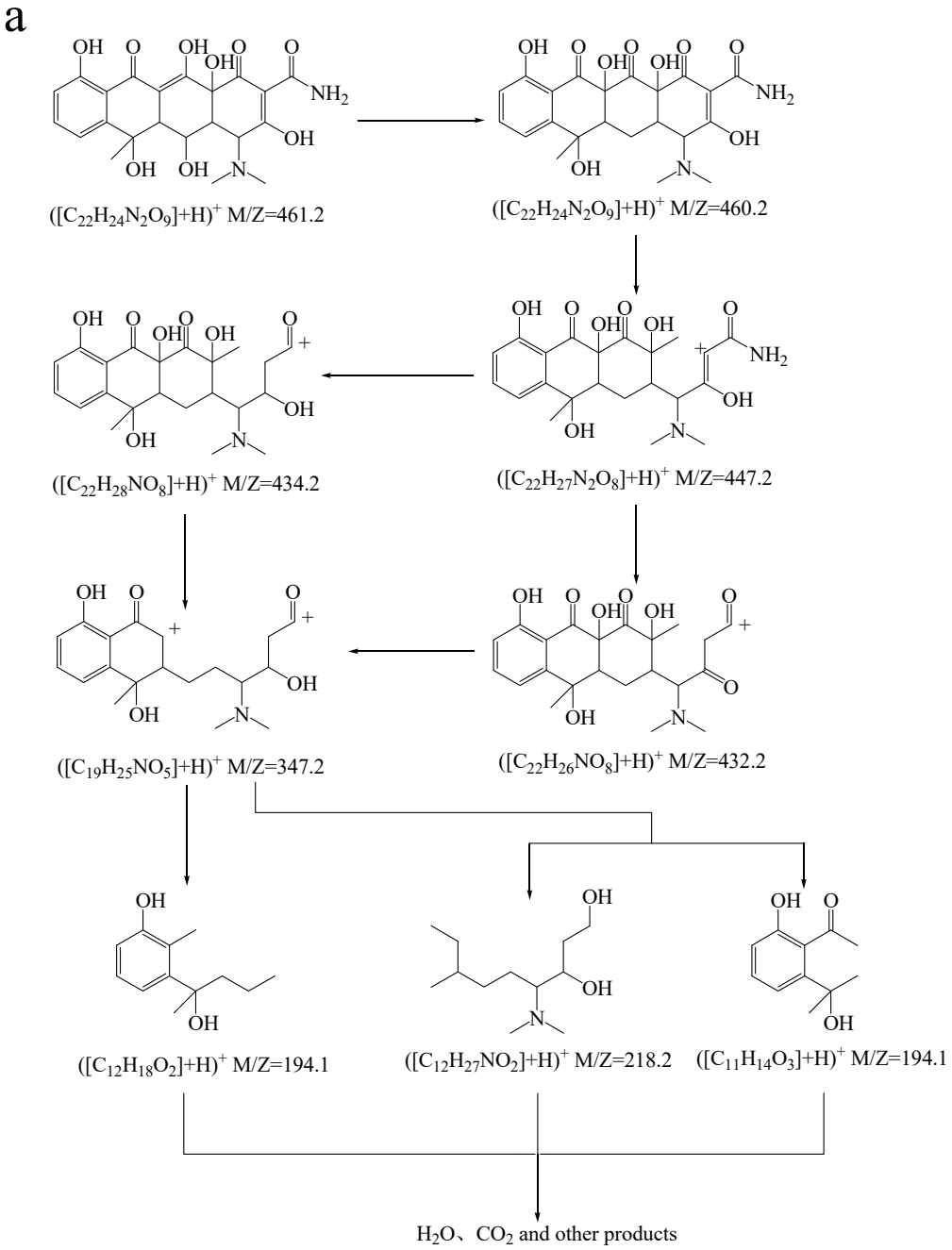

Figure 7. *Cont.*

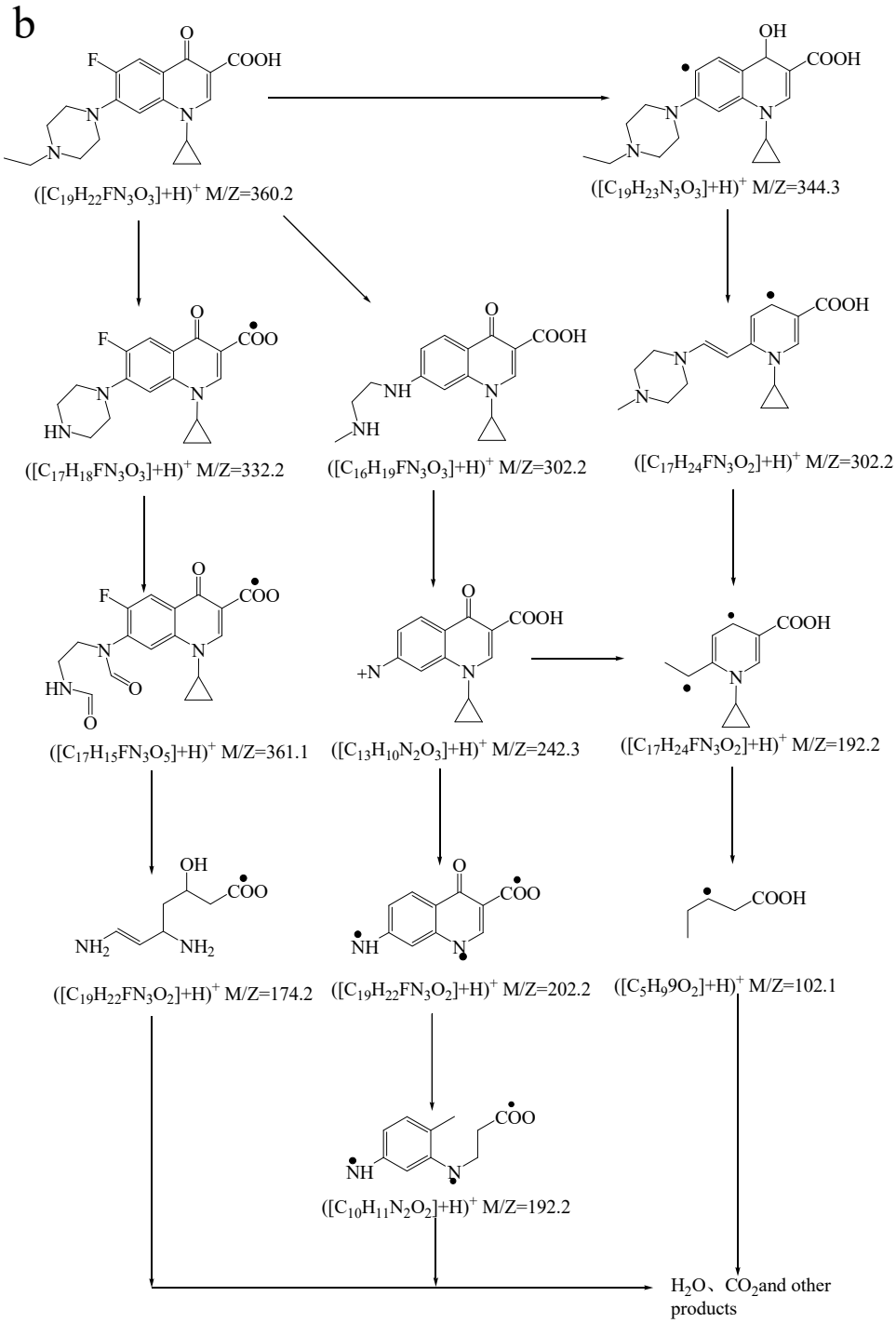

Figure 7. The possible degradation pathway for (**a**) OTC, (**b**) ENR.

In addition, in spherical Co_3O_4{110} and flower-shaped Co_3O_4{111} aqueous suspensions, PMS was not only reduced to SO_4^-• (Equation (7)) but also oxidized to large amounts of SO_5^-• (Equation (9)) due to the decomposition of PMS following the classic Fenton reaction mechanism. Thus, with the oxidation from Co(II) to Co(III), the value of Co(II)/Co(III) [spherical Co_3O_4{110}, flower-shape Co_3O_4{111}] decreased from 1.36 to 1.16 obviously after cycled uses (Figure 6f). Meanwhile, the accumulated Co(III) was reduced by PMS with the generation of SO_5^-• in dispersions of flower-shaped Co_3O_4{111} and spherical Co_3O_4{110}, resulting in a low selective PMS conversion to sulfate radicals. Different from spherical Co_3O_4{110} and flower-shaped Co_3O_4{111} aqueous suspensions, PMS was mainly reduced to SO_4^-• and OH• by the Co(II) and C-dots in the aqueous

suspension of flower-shaped C-dots/Co_3O_4{111}. Although some Co(II) was oxidized to Co(III) by PMS with the generation of SO_4^{-}• and OH• (Equations (6) and (7)), R• could transfer the electron to Co (III) for its quick reduction via Co–O–C linkage, resulting in a stable value of Co(II)/Co(III) [flower-shaped C-dots/Co_3O_4{111}] before and after catalytic reaction (Figure 6f). Thus, such different mechanism of PMS activation over Co_3O_4 and flower-shaped Co_3O_4{111} led to higher selective PMS conversion to SO_4^{-}• over flower-shaped C-dots/Co_3O_4{111}.

Table 3. The reaction rate constants of ethanol (EtOH) and tert-Butanol (TBA) with hydroxyl radical and sulfate radical.

Radical Probo	Reaction Rate Constant (M^{-1} S^{-1})	
	SO_4^{-}•	OH•
Ethanol (EtOH)	(1.6–7.7) × 10^7	(1.2–2.8) × 10^9
Tert-Butanol (TBA)	(4–9.1) × 10^5	(3.8–7.6) × 10^8

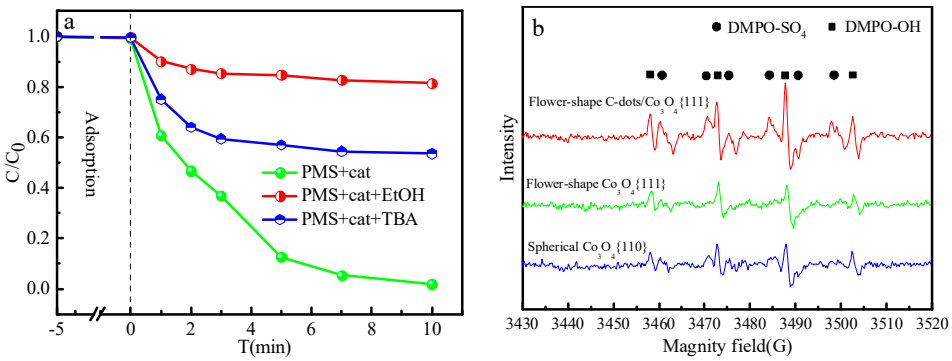

Figure 8. (**a**) Degradation of ENR in the system of PMS and flower-shaped C-dots/Co_3O_4{111} in the presence of TBA or EtOH; (**b**) EPR spectra in various conditions. Center field: 34,800 G; microwave frequency: 9.849 GHz; modulation frequency: 100 kHz; and power: 20.17 mW. ■ DMPO-OH; •DMPO-SO_4.

In order to further illustrate the co-catalyst effect of C-dots on Co_3O_4{111}, PMS activation rate per second on a single active site was calculated. In classic Fenton reaction system, the concentration of OH• in the aqueous dispersion with H_2O_2 could be directly measured by using the terephthalic acid (TPA) probe method. Accordingly, the turnover frequencies (TOF) of Fenton catalyst could be obtained from the conversion number of H_2O_2 into OH• per second on a single active site [40]. However, TOF cannot be calculated in PMS activation system because it is difficult to accurately quantify the SO_4^{-}•. Thus, the turnover numbers (TONs) are selected to evaluate the catalytic efficiency for PMS activation (Equation (3)) [41].

$$\text{TONs} = \text{n (converted reactants)/n (catalyst active sites)}. \quad (3)$$

The number of active sites of catalysts can be calculated by the following method [42]:

$$n = \frac{\text{catalyst surface area}}{\text{unit cell area}} \times \frac{Co^{2+}}{Co^{3+}}. \quad (4)$$

The specific surface area and Co^{2+}/Co^{3+} of the catalyst can be obtained by BET and XPS spectra, respectively. Moreover, the unit cell area can be calculated by the length of Co_3O_4 cell [42]. Then, the PMS concentration was obtained by low-concentration iodide methods (ESI). As expected, C-dots/Co_3O_4{111} show higher TONs than Co_3O_4{111} (Figure S11). Such improvement can be explained as follows: Besides of PMS reduction to SO_4^{-}• by Co(II), graphene structure of C-dots could facilitate the production of R• (R•,

the product of SO_4^{-}•/OH• attacking to organics) (Equation (10)). Such reactive organic radicals promote the PMS conversion to SO_4^{-}• (Equation (11)). Electrons were not only transferred from R• to Co(III) via the Co–O–C linkage for Co(III) reduction to Co(II), but also transferred from R• to PMS over C-dots with the generation of SO_4^{-}• (Equation (12)). Thus, the PMS conversion rate is obviously increased after C-dots doped on Co_3O_4{111}.

Based on the above results, the possible catalytic mechanism of flower-shape C-dots/Co_3O_4{111} is proposed (Figure 9). Both Co_3O_4 crystal structure and doped C-dots played an important role in PMS activation. On the one hand, flower-shaped C-dots/Co_3O_4{111} exposed more Co(II) for PMS activation with generation of SO_4^{-}•. On the other hand, graphene structure of C-dots facilitated the production of reactive organic radicals (R•) (Equation (10)). Some of electrons are transferred from R• to Co(III) via the Co–O–C linkage with the reduction of Co(III) to Co(II) (Equation (11)), which decrease the 'invalid decomposition' of PMS (Equation (9)). Other electrons are transferred from R• to PMS over C-dots with the generation of SO_4^{-}• (Equation (12)) (R* is the intermediate product from the reaction of R• and Co(III)/HSO_5^{-}). Thus, there were three electron transfer routes in the catalytic process: the first route was from Co(II) to PMS with the generation of SO_4^{-}•, the second route was from R• to Co(III) via the Co–O–C linkage with the quick reduction of Co(III) to Co(II), and the third route was from R• to PMS via C-dots with the generation of SO_4^{-}•. Consequently, high catalytic activity and selective PMS conversion to SO_4^{-}• was achieved.

$$\text{Co(II)} + HSO_5^{-} \rightarrow \text{Co(III)} + SO_4^{2-} + \text{OH}\bullet, \quad (5)$$

$$\text{Co(II)} + HSO_5^{-} \rightarrow \text{Co(III)} + SO_4^{-}\bullet + OH^{-}, \quad (6)$$

$$\text{OH}\bullet + SO_4^{2-}/HSO_4^{-} \leftrightarrow SO_4^{-}\bullet/HSO_4\bullet + OH^{-}, \quad (7)$$

$$\text{Co(III)} + HSO_5^{-} \rightarrow \text{Co(II)} + SO_5^{-}\bullet + H^{+}, \quad (8)$$

$$R + SO_4^{-}\bullet/\text{OH}\bullet \rightarrow R\bullet + SO_4^{2-}/H_2O, \quad (9)$$

$$R\bullet + \text{Co(III)-O-C-dots} \rightarrow R^{*} + \text{Co(II)-O-C-dots}, \quad (10)$$

$$R\bullet + HSO_5^{-} \rightarrow R^{*} + SO_4^{-}\bullet, \quad (11)$$

$$\text{OH}\bullet/SO_4^{-}\bullet + \text{OTC/ENR} \rightarrow SO_4^{2-} + CO_2 + H_2O. \quad (12)$$

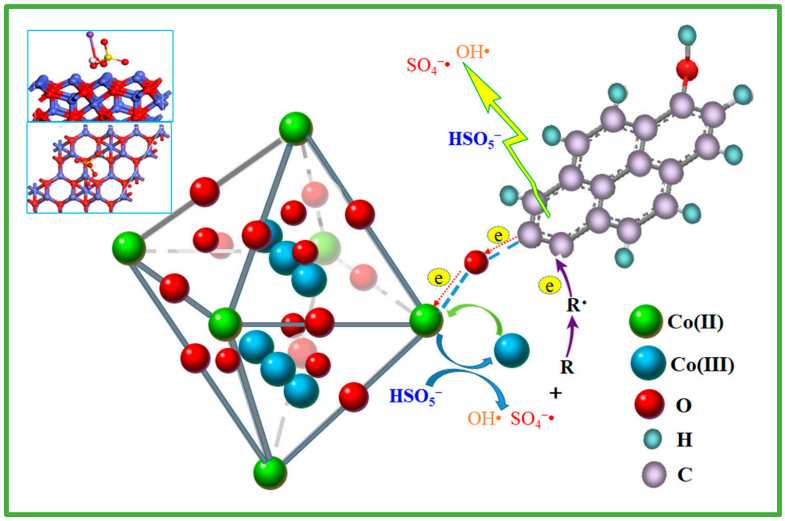

Figure 9. The possible catalytic mechanisms in the suspension of PMS and flower-shaped C-dots/Co_3O_4{111}.

3. Materials and Methods

3.1. Chemicals

All chemicals were analytical grade and used without further purification. 5,5-Dimethyl-1-pyrroline N-oxide (DMPO) and Oxone ($KHSO_5 \cdot 0.5KHSO_4 \cdot 0.5K_2SO_4$, ≥95% purity) were purchased from Shanghai Macklin Biochemical Co. Ltd (Shanghai, China). Oxytetracycline (OTC, ≥99%), Enrofloxacin (ENR, ≥99%), Rhodamine B (Rh B, ≥99%), and Methyl orange (MO, ≥99%) were purchased from the Aladdin Industrial Corporation. (Shanghai, China). Acetonitrile (99.9% purity) hypergrade for LC-MS was supplied from the Tedia Company.(Fairfield, OH, USA) Tetrabutylammonium bromide (TBAb, ≥99.0%) was obtained from Aladdin Chemistry Co. Ltd. (Shanghai, China). Other reagents including methanol (99.5%), ethanol (99.7%), acetic acid, tert-Butanol (TBA ≥99.0%), Cobalt acetate $Co(CH_3COO)_2 \cdot 4H_2O$, and Cetrimonium Bromide (CTMAB ≥99.0%) were purchased from Nanjing Chemical Reagent Co. LTD (Nanjing, China).

3.2. Synthesis of Catalysts

C-dots: The synthesis method of C-dots is presented in a previous article [43]. Two grap hite rods were inserted in a beaker containing 400 mL ultrapure water as two electrodes and the DC voltage of 30 V were attached at both ends of the electrode under continuous stirring. Five days later, the graphite rods were corrode and the water in the beaker turned black. Then, the large particles in the solution were filtered out with a filter paper. The solution was centrifuged with high speed centrifuge at 15,000 rpm for 30 min to remove the small particles. Finally, the solution was evaporated at 60 °C, and C-dots was obtained.

Flower-shaped C-dots/Co_3O_4{111}: Synthesis processes of catalysts are shown as following method in Figure S12. A total of 1.192 g $Co(CH_3COO)_2 \cdot 4H_2O$ was dissolved in 60 mL ethanol containing a certain amount of C-dots. Then, CTMAB ($Co(CH_3COO)_2 \cdot 4H_2O$: CTMAB = 2:1) was added into the above solution, and the mixture was stirred at 120 rpm for 15 min. The mixture was transferred to a Teflon-lined stainless steel autoclave and then heated in a high temperature oven at 170 °C for 48 h. The solid product was dried at 80 °C for 12 h to obtain C-dots/Co_3O_4{111}. The synthesis process of flower-shaped Co_3O_4{111} was similar to C-dots/Co_3O_4{111}, except that C-dots were not added into the hydrothermal reaction system. As for spherical Co_3O_4, C-dots and CTMAB are not added.

3.3. Characterization of Catalysts

The surface morphology of the material is characterized by field emission scanning electron microscopy (FESEM, S-3400NII, Hitachi, Tokyo, Japan). Microstructure and diffraction patterns were characterized by transmission electron microscopy (TEM, JEM-200CX, JEOL, Tokyo, Japan). Furthermore, the specific surface area and pore structure of catalysts were measured by Micromeritics Instrument (Nova 3000, Quantachrome).

The crystal structure of catalysts was characterized by the X-ray diffraction (XRD, Cu-Kα radiation, λ = 1.540562 Å, X'TRA, ARL, Switzerland). The XRD patterns were tested in the range of 30–70° (2θ). The binding energies of Co of the catalyst were measured by X-ray photoelectron spectroscopy (PHI 5000 Versa Probe, UlVAC-PHI, Chigasaki, Japan). In addition, the Fourier Transform Infrared Spectrometer (FT-IR, NEXUS870, NICOLET, Wilmington, NC, USA) was used to analyze the chemical structural functional groups.

To analyze the redox properties of Co in catalyst composites, the H_2-TPR experiments were conducted on the chemisorption analyzer (2920, AutoChem II, Micromeritics). The samples were heated to 400 °C in the Ar atmosphere for 60 min. After cooling down to 50 °C, the samples were heated to 900 °C with temperature ramp of 10 °C min^{-1} in 10% H_2/Ar. Electrochemical impedance test was carried out by using CHI 760D electrochemical workstation (Austin, TX, USA).

Electrochemical measurements were conducted by an electrochemical workstation (CHI660D Instruments) with a standard three-electrode system. A total of 0.01 g catalyst was ultrasonic dispersed in 1 mL chitosan solution (0.05 M), then the dispersed droplets were placed on the glass electrode and dried in a vacuum oven before use.

DMPO-trapped EPR signals were detected in different aqueous dispersions of the corresponding samples with and without the addition of PMS. A detailed information for the recorded EPR signals is provided in the Figure S10.

3.4. Catalytic Performance

Four aromatic pollutants (OTC, ENR, MB, and Rh B) were selected to evaluate the catalysts activity. Preliminary experiments for ENR degradation indicated that the optimal doses of the catalyst and PMS were 0.05 g/L and 12.5 mM, respectively (Figure 6). Thus, these two doses were used in all catalytic degradation experiments unless otherwise specified. Typically, 200 mL aqueous solutions with certain pollutant and 0.01 g catalyst were placed in 250 mL beaker flasks. To ensure the adsorption–desorption equilibrium, the suspensions were magnetically stirred for 30 min before the catalytic reaction. Then, 12.5 mM PMS was added in the suspensions with magnetic stirring (120 rpm). At given time intervals, 2 mL aliquots were sampled and followed by adding methanol into the sample to quench the radicals for termination of the catalytic reaction, and subsequently filtrated through a Millipore filter (pore size 0.45 μm) prior to the analysis. In addition, to test the catalytic stability, the catalyst was recovered by filtration, washed with deionized water, dried, and reused in the following cycle. The degradation rate of pollutants is calculated. Concentrations of OTC and ENR were measured using Agilent 1200 HPLC (Agilent Technologies, Palo Alto, CA, USA) equipped with a quaternary pump and a UV detector. Chromatographic analysis was performed by a reversed-phase C-18 column (4.6 × 150 mm, 5 μm particle diameter), and the specific liquid conditions are listed in Table S2. The degradation intermediates of OTC and ENR were detected by HPLC coupled with time-of-flight mass spectrometry detection (HPLC–TOFMS, Agilent 1290 Infinity LC/6460 QQQ MS) in positive polarity. Rh B and MB concentrations in solutions were analyzed by the UV−1800 UV–vis spectrometer (Shimadzu, Japan).

4. Conclusions

Novel flower-shaped C-dots/Co_3O_4{111} were constructed for the improvement of the catalytic activity and selective peroxymonosulfate (PMS) conversion to sulfate radicals. Being attributed to the exposure of {111} facets, C-dots/Co_3O_4{111} could provide plenty of Co(II) for PMS activation. In addition, the Co_3O_4{111} facet not only possessed high adsorption energy of PMS on catalyst, but also facilitated the electron transfer from Co(II) to PMS. On the other hand, the graphene structure of C-dots facilitated the production of reactive organic radicals (R•), which provided the electrons for Co(III) and PMS reduction. Thus, C-dots doped on Co_3O_4{111} could obviously enhance the TONs. The catalytic degradation tests indicated that antibiotics and dyes could be efficiently degraded over flower-shaped C-dots/Co_3O_4{111}. Even after six cycling runs, flower-shaped C-dots/Co_3O_4{111} still remained a high catalytic activity. Additionally, according to degradation intermediates identified by LC-MS/TOF and electron cloud density calculated by Gaussian program calculation, the possible degradation pathways of OTC/ENR were proposed. EPR spectra and radical capture experiments further demonstrated that both OH• and SO_4^{-}• played a dominant role in catalytic degradation processes. Thus, the present work provided a simple and efficient way for PMS activation, which could be applied in the treatment of wastewater.

Supplementary Materials: The following are available online at https://www.mdpi.com/2073-4344/11/1/135/s1, Figure S1. Co2p peaks of (a) flower-shape C-dots/Co_3O_4{111} before reaction, (b) flower-shape C-dots/Co_3O_4{111} after reaction (c) flower-shape Co_3O_4{111} before reaction, (d) flower-shape Co_3O_4{111} after reaction. Figure S2. TPR results of flower-like Co_3O_4 doped with different carbon quantum dots. Figure S3. Influence of different conditions on ENR degradation over flower-shape C-dots/Co_3O_4{111}: (a) catalyst dosage (pH = 7.00, 0.3 mM PMS, 25 °C), (b) PMS dosage (pH = 7.00, 0.05 g/L catalyst dosage, 25 °C), (c) temperature (pH = 7.00, 0.3 mM PMS, 0.05 g/L catalyst dosage), (d) pH (0.3 mM PMS, 0.05 g/L catalyst dosage, 25 °C). Figure S4. Co leaching during different pH conditions in flower-shape C-dots/Co_3O_4{111}/PMS/ENR system.

Figure S5. Density functional theory (DFT) calculations of PMS on different crystalline planes of Co_3O_4. Figure S6. Frontier electron densities of OTC and ENR calculated by Gaussian. Figure S7. Iron spectra at different retention time (RT) of OTC catalysis sample. Figure S8. Iron spectra at different retention time (RT) of ENR catalysis sample. Figure S9. TOC removal under different reaction conditions. Figure S10. EPR spectra in various conditions. Center field: 34,800 G; microwave frequency: 9.849 GHz; modulation frequency: 100 kHz; and power: 20.17 mW. Figure S11. The turnover numbers(TONs) of different catalysts prepared (Firstly, 10 mM potassium iodide (KI) solution was prepared to dilute the PMS sample 50 times. Then the solution was shaken for 5 minutes and detected with UV–vis spectrometer at λ = 352 nm). Figure S12. Schematic of synthesize process of flower-shape C-dots/Co_3O_4{111}. Table S1. The pseudo-first-order kinetic equations, rate constants (K) and regression coefficients (R^2) of degradation of OTC/ENR over different catalysts. Table S2. Operating conditions for HPLC about OTC and ENR.

Author Contributions: Conceptualization, J.W.; data curation, Z.W., Q.Z., and L.C.; formal analysis, S.Z.; investigation, Z.W., Q.Z. and J.Z.; methodology, J.Z.; project administration, J.W.; software, W.B.; supervision, J.W.; validation, A.L.; writing—original draft, Z.W. and Q.Z.; writing—review & editing, J.W. All authors have read and agreed to the published version of the manuscript.

Funding: This research was supported by National Natural Science Foundation of China (No. 51878335 and No. 52070095), Natural Science Foundation of Jiangsu province (BK091255) and Water Resource Research Project of Jiangsu province (2017043).

Institutional Review Board Statement: Not applicable.

Informed Consent Statement: Not applicable.

Data Availability Statement: The data presented in this study are available openly.

Conflicts of Interest: The authors declare no conflict of interest.

References

1. Hu, P.; Long, M. Cobalt-catalyzed sulfate radical-based advanced oxidation: A review on heterogeneous catalysts and applications. *Appl. Catal. B Environ.* **2016**, *181*, 103–117. [CrossRef]
2. Pi, Y.; Ma, L.; Zhao, P.; Cao, Y.; Gao, H.; Wang, C.; Sun, J.; Dong, S.; Li, Q. Facile green synthetic graphene-based Co-Fe Prussian blue analogues as an activator of peroxymonosulfate for the degradation of levofloxacin hydrochloride. *J. Colloid Interface Sci.* **2018**, *526*, 18–27. [CrossRef] [PubMed]
3. Wang, Y.; Liu, C.; Zhang, Y.; Meng, W.; Yu, B.; Pu, S.; Yuan, D.; Qi, F.; Xu, B.; Chu, W. Sulfate radical-based photo-Fenton reaction derived by $CuBi_2O_4$ and its composites with α-Bi_2O_3 under visible light irradiation: Catalyst fabrication, performance and reaction mechanism. *Appl. Catal. B Environ.* **2018**, *235*, 264–273. [CrossRef]
4. Lyu, L.; Zhang, L.; Wang, Q.; Nie, Y.; Hu, C. Enhanced Fenton Catalytic Efficiency of gamma-Cu-Al_2O_3 by sigma-Cu^{2+}-Ligand Complexes from Aromatic Pollutant Degradation. *Environ. Sci. Technol.* **2015**, *49*, 8639–8647. [CrossRef] [PubMed]
5. Hammouda, S.B.; Zhao, F.; Safaei, Z.; Ramasamy, D.L.; Doshi, B.; Sillanpää, M. Sulfate radical-mediated degradation and mineralization of bisphenol F in neutral medium by the novel magnetic Sr_2CoFeO_6 double perovskite oxide catalyzed peroxymonosulfate: Influence of co-existing chemicals and UV irradiation. *Appl. Catal. B Environ.* **2018**, *233*, 99–111. [CrossRef]
6. Li, X.; Wang, Z.; Zhang, B.; Rykov, A.I.; Ahmede, M.A.; Wang, J. $Fe_xCo_{3-x}O_4$ nanocages derived from nanoscale metal–organic frameworks for removal of bisphenol A by activation of peroxymonosulfate. *Appl. Catal. B Environ.* **2016**, *181*, 788–799. [CrossRef]
7. Rajeshkhanna, G.; Umeshbabu, E.; Ranga Rao, G. Charge storage, electrocatalytic and sensing activities of nest-like nanostructured Co_3O_4. *J. Colloid Interface Sci.* **2017**, *487*, 20–30. [CrossRef]
8. Song, K.; Cho, E.; Kang, Y.-M. Morphology and Active-Site Engineering for Stable Round-Trip Efficiency Li–O_2 Batteries: A Search for the Most Active Catalytic Site in Co_3O_4. *ACS Catal.* **2015**, *5*, 5116–5122. [CrossRef]
9. Qin, C.; Hou, B.; Wang, J.; Wang, Q.; Wang, G.; Chen, C.; Jia, L.; Li, D. Crystal-Plane-Dependent Fischer–Tropsch Performance of Cobalt Catalysts. *ACS Catal.* **2018**, *8*, 9447–9455. [CrossRef]
10. Spezzati, G.; Benavidez, A.D.; Delariva, A.T.; Su, Y.; Hensen, E.J.M.; Hofmann, J.P.; Asahinac, S.; Olivier, E.J.; Neethling, J.H.; Miller, J.T. CO oxidation by Pd supported on CeO_2(100) and CeO_2(111) facets. *Appl. Catal. B Environ.* **2019**, *243*, 36–46. [CrossRef]
11. Xu, S.; Zhu, H.; Cao, W.; Wen, Z.; Wang, J.; François-Xavier, C.P.; Wintgens, T. Cu-Al_2O_3-g-C_3N_4 and Cu-Al_2O_3-C-dots with dual-reaction centres for simultaneous enhancement of Fenton-like catalytic activity and selective H_2O_2 conversion to hydroxyl radicals. *Appl. Catal. B Environ.* **2018**, *234*, 223–233. [CrossRef]
12. Zubir, N.A.; Yacou, C.; Motuzas, J.; Zhao, X.S.; Diniz Da Costa, J.C. The sacrificial role of graphene oxide in stabilising a Fenton-like catalyst GO-Fe_3O_4. *Chem. Commun.* **2015**, *51*, 9291–9293. [CrossRef] [PubMed]
13. Xiao, Y.; Liu, S.; Fang, S.; Jia, D.; Su, H.; Zhou, W.; Wiley, J.B.; Li, F. Plum-like and octahedral Co_3O_4 single crystals on and around carbon nanotubes: Large scale synthesis and formation mechanism. *RSC Adv.* **2012**, *2*, 3496. [CrossRef]

14. Shinde, S.L.; Ishii, S.; Dao, T.D.; Takei, T.; Sugvaneshwar, R.P.; Nanda, K.K.; Nagao, T. Enhanced Solar Light Absorption and Photoelectrochemical Conversion Using TiN Nanoparticle-Incorporated C_3N_4-C Dot Sheets. *ACS Appl. Mater. Interfaces* **2018**, *10*, 2460–2468. [CrossRef] [PubMed]
15. Zhang, H.; Wu, W.; Li, Y.; Wang, Y.; Zhang, C.; Zhang, W.; Wang, L.; Niu, L. Enhanced photocatalytic degradation of ciprofloxacin using novel C-dot@Nitrogen deficient g-C_3N_4: Synergistic effect of nitrogen defects and C-dots. *Appl. Surf. Sci.* **2019**, *465*, 450–458. [CrossRef]
16. Wang, L.; Yan, D.; Lyu, L.; Hu, C.; Jiang, N.; Zhang, L. Notable light-free catalytic activity for pollutant destruction over flower-like BiOI microspheres by a dual-reaction-center Fenton-like process. *J. Colloid Interface Sci.* **2018**, *527*, 251–259. [CrossRef]
17. Lu, Y.; Zhan, W.; He, Y.; Wang, Y.; Kong, X.; Kuang, Q. MOF-templated synthesis of porous Co_3O_4 concave nanocubes with high specific surface area and their gas sensing properties. *ACS Appl. Mater. Interfaces* **2014**, *6*, 4186–4195. [CrossRef]
18. Kang, M.; Kang, M.; Zhou, H.; Wu, D.; Lv, B. Systematic shape evolution of Co_3O_4 nanocrystals from octahedra to spheres under the influence of ${C_2O_4}^{2-}$ and PVP. *CrystEngComm* **2016**, *18*, 9299–9306. [CrossRef]
19. Okeyoshi, K.; Shinhama, T.; Budpud, K.; Joshi, G.; Okajima, M.K.; Kaneko, T. Micelle-Mediated Self-Assembly of Microfibers Bridging Millimeter-Scale Gap to Form. Three-Dimensional-Ordered Polysaccharide Membranes. *Langmuir* **2018**, *34*, 13965–13970.
20. Zeng, X.; Wang, Z.; Meng, N.; Mccarthy, D.T.; Deletic, A.; Pan, J.H. Highly dispersed TiO_2 nanocrystals and carbon dots on reduced graphene oxide: Ternary nanocomposites for accelerated photocatalytic water disinfection. *Appl. Catal. B Environ.* **2017**, *202*, 33–41. [CrossRef]
21. He, M.; He, M.; Zhang, P.; Xu, S.; Yan, X. Morphology Engineering of Co_3O_4 Nanoarrays as Free-Standing Catalysts for Lithium-Oxygen Batteries. *ACS Appl. Mater. Interfaces* **2016**, *8*, 23713–23720. [CrossRef] [PubMed]
22. Ren, Y.; Lin, L.; Fan, J.; Yang, Z. Sulfate radicals induced from peroxymonosulfate by magnetic ferrospinel MFe_2O_4 (M = Co, Cu, Mn, and Zn) as heterogeneous catalysts in the water. *Appl. Catal. B Environ.* **2015**, *165*, 572–578. [CrossRef]
23. Mansournia, M.; Rakhshan, N. Hydrothermal synthesis and tuning of size and morphology of α-$Co(OH)_2$ and α-$Co_2(OH)_3Cl$ nanostructures as precursors for nanosized Co_3O_4. *Ceram. Int.* **2017**, *43*, 7282–7289. [CrossRef]
24. Ding, Y.; Chen, M.; Wu, K.; Chen, M.; Sun, L.; Liu, Z.; Shi, Z.; Liu, Q. High-performance peroxidase mimics for rapid colorimetric detection of H_2O_2 and glucose derived from perylene diimides functionalized Co_3O_4 nanoparticles. *Mater. Sci. Eng. C* **2017**, *80*, 558–565. [CrossRef]
25. Shang, Z.; Zhan, W.; Sun, M.; Guo, Y. Activity and stability of Co_3O_4-based catalysts for soot oxidation: The enhanced effect of Bi_2O_3 on activation and transfer of oxygen. *Appl. Catal. B Environ.* **2017**, *209*, 33–44. [CrossRef]
26. Jácome-Acatitla, G.; Tzompantzi, F.; López-González, R.; García-Mendoza, C.; Alvaro, J.M.; Gómez, R. Photodegradation of sodium naproxen and oxytetracycline hydrochloride in aqueous medium using as photocatalysts Mg-Al calcined hydrotalcites. *J. Photochem. Photobiol. A Chem.* **2014**, *277*, 82–89. [CrossRef]
27. Ezzariai, A.; Riboul, D.; Lacroix, M.Z.; Barret, M.; El Fels, L.; Merlina, G. A pressurized liquid extraction approach followed by standard addition method and UPLC-MS/MS for a fast multiclass determination of antibiotics in a complex matrix. *Chemosphere* **2018**, *211*, 893–902. [CrossRef]
28. Wang, J.; Boyi, Z.; Ruijia, G.; Tian-Shun, S.; Jinping, Y.; Jingjing, X. Degradation characterization and pathway analysis of chlortetracycline and oxytetracycline in a microbial fuel cell. *RSC Adv.* **2018**, *8*, 28613–28624. [CrossRef]
29. Chen, Q.; Wu, S.; Xin, Y. Synthesis of Au–CuS–TiO_2 nanobelts photocatalyst for efficient photocatalytic degradation of antibiotic oxytetracycline. *Chem. Eng. J.* **2016**, *302*, 377–387. [CrossRef]
30. Albero, B.; Luis Tadeo, J.; Escario, M.; Miguel, E.; Ana Perez, R. Persistence and availability of veterinary antibiotics in soil and soil-manure systems. *Sci. Total Environ.* **2018**, *643*, 1562–1570. [CrossRef]
31. Matta, M.K.; Chockalingam, A.; Gandhi, A.; Stewart, S.; Xu, L.; Shea, K. LC-MS/MS based quantitation of ciprofloxacin and its application to antimicrobial resistance study in Balb/c mouse plasma, urine, bladder and kidneys. *Anal. Methods* **2018**, *10*, 1237–1246. [CrossRef]
32. Ferrey, M.L.; Coreen Hamilton, M.; Backe, W.J.; Anderson, K.E. Pharmaceuticals and other anthropogenic chemicals in atmospheric particulates and precipitation. *Sci. Total Environ.* **2018**, *612*, 1488–1497. [CrossRef] [PubMed]
33. Chung, H.S.; Lee, Y.J.; Rahman, M.M.; Abd El-Aty, A.M.; Lee, H.S.; Kabir, M.H. Uptake of the veterinary antibiotics chlortetracycline, enrofloxacin, and sulphathiazole from soil by radish. *Sci. Total Environ.* **2017**, *605–606*, 322–331. [CrossRef] [PubMed]
34. Wei, M.; Gao, L.; Li, J.; Fang, J.; Cai, W.; Li, X.; Xu, A. Activation of peroxymonosulfate by graphitic carbon nitride loaded on activated carbon for organic pollutants degradation. *J. Hazard. Mater.* **2016**, *316*, 60–68. [CrossRef] [PubMed]
35. Zhang, J.; Zhao, X.; Wang, Y.; Gong, Y. Peroxymonosulfate-enhanced visible light photocatalytic degradation of bisphenol A by perylene imide-modified g-C_3N_4. *Appl. Catal. B Environ.* **2018**, *237*, 976–985. [CrossRef]
36. Chen, X.; Oh, W.D.; Hu, Z.T.; Sun, Y.M.; Webster, R.D.; Li, S.Z. Enhancing sulfacetamide degradation by peroxymonosulfate activation with N-doped graphene produced through delicately-controlled nitrogen functionalization via tweaking thermal annealing processes. *Appl. Catal. B Environ.* **2018**, *225*, 243–257. [CrossRef]
37. Gong, C.; Chen, F.; Yang, Q.; Luo, K.; Yao, F.; Wang, S.; Wang, X.; Wu, J.; Li, X.; Wang, D.; et al. Heterogeneous activation of peroxymonosulfate by Fe-Co layered doubled hydroxide for efficient catalytic degradation of Rhoadmine B. *Chem. Eng. J.* **2017**, *321*, 222–232. [CrossRef]
38. Ma, W. One-step synthesis of novel Fe_3C@nitrogen-doped carbon nanotubes/graphene nanosheets for catalytic degradation of Bisphenol A in the presence of peroxymonosulfate. *Chem. Eng. J.* **2019**, *356*, 1022–1031. [CrossRef]

39. Wang, Y.; Sun, H.; Ang, H.M.; Moses, O.T.; Wang, S. 3D-hierarchically structured MnO_2 for catalytic oxidation of phenol solutions by activation of peroxymonosulfate: Structure dependence and mechanism. *Appl. Catal. B Environ.* **2015**, *164*, 159–167. [CrossRef]
40. Jia, Q.; Jia, Q.; Ramaswamy, N.; Tylus, U.; Strickland, K.; Li, J.; Serov, A. Spectroscopic insights into the nature of active sites in iron–nitrogen–carbon electrocatalysts for oxygen reduction in acid. *Nano Energy* **2016**, *29*, 65–82. [CrossRef]
41. Costentin, C.; Costentin, C.; Drouet, S.; Robert, M.; Saveant, J.M. Turnover numbers, turnover frequencies, and overpotential in molecular catalysis of electrochemical reactions. Cyclic voltammetry and preparative-scale electrolysis. *J. Am. Chem. Soc.* **2012**, *134*, 11235–11242. [CrossRef] [PubMed]
42. Blakemore, J.D.; Blakemore, J.D.; Gray, H.B.; Winkler, J.R.; Müller, A.M. Co_3O_4 Nanoparticle Water-Oxidation Catalysts Made by Pulsed-Laser Ablation in Liquids. *ACS Catal.* **2013**, *3*, 2497–2500. [CrossRef]
43. Ming, H.; Ma, Z.; Liu, Y.; Pan, K.; Yu, H.; Wang, F.; Kang, Z. Large scale electrochemical synthesis of high quality carbon nanodots and their photocatalytic property. *Dalton Trans.* **2012**, *41*, 9526–9531. [CrossRef] [PubMed]